



Investigation of subgrains in directionally solidified cast mono-seeded silicon and their interactions with twin boundaries

Maike Becker, Etienne Pihan, Fabrice Guittonneau, Laurent Barrallier, Gabrielle Regula, Hadjer Ouaddah, Guillaume Reinhart, Nathalie Mangelinck-Noël

► To cite this version:

Maike Becker, Etienne Pihan, Fabrice Guittonneau, Laurent Barrallier, Gabrielle Regula, et al.. Investigation of subgrains in directionally solidified cast mono-seeded silicon and their interactions with twin boundaries. *Solar Energy Materials and Solar Cells*, 2020, 218, pp.110817. <hal-03169396>

HAL Id: hal-03169396

<https://hal.science/hal-03169396v1>

Submitted on 15 Mar 2021

HAL is a multi-disciplinary open access archive for the deposit and dissemination of scientific research documents, whether they are published or not. The documents may come from teaching and research institutions in France or abroad, or from public or private research centers.

L'archive ouverte pluridisciplinaire **HAL**, est destinée au dépôt et à la diffusion de documents scientifiques de niveau recherche, publiés ou non, émanant des établissements d'enseignement et de recherche français ou étrangers, des laboratoires publics ou privés.



HAL Authorization

Investigation of subgrains in directionally solidified cast mono-seeded silicon and their interactions with twin boundaries

Maike Becker^{a,*1}, Etienne Pihan^b, Fabrice Guittonneau^c, Laurent Barrallier^c, Gabrielle Regula^a, Hadjer Ouaddah^a, Guillaume Reinhart^a, Nathalie Mangelinck-Noël^a

^a Aix Marseille Univ, Université de Toulon, CNRS, IM2NP, 13397, Marseille, France

^b Univ. Grenoble Alpes, INES, CEA, LITEN, Department of Solar Technologies, F-73375 Le Bourget du Lac, France

^c Arts et Métiers Paristech/Institut Carnot Arts Centre Aix-en-Provence 2, Cours des Arts et Métiers, 13617, Aix-en-Provence, Cedex 1, France

*email: maike.becker@dlr.de

¹ Present address: Institut für Materialphysik im Weltraum, Deutsches Zentrum für Luft- und Raumfahrt, 51170 Köln, Germany

Keywords: silicon; cast mono; subgrain boundaries; dislocations; X-ray diffraction imaging; electron backscatter diffraction

Abstract

Directional solidification of a cast mono-seed and of a FZ-seed was performed and the grain and defect structures of the seeds as well as of the regrown parts are analyzed. *In situ* X-ray diffraction imaging enabled the observation of the dislocation arrangements. During the heating process, in the FZ-seed, mobile dislocations glide on $\{111\}$ planes, whereas in the cast mono seed dislocations are arranged in a mainly immobile cellular structure. *Ex situ* grain orientation mappings reveal the presence of subgrains with misorientations up to 3° in the regrown part of the cast mono-seeded sample, which are not observed in the regrown part of the FZ-seeded sample. Subgrain boundaries characterized by misorientations around the $[001]$ growth axis propagate roughly along the growth axis and increase their misorientation by merging with new subgrain boundaries appearing in their vicinity. Although the first inception of subgrain formation cannot be revealed, the comparison of the dislocation arrangements in the two seeds strongly suggests an influence of the latter on subgrain formation. In the regrown part, interactions between subgrain boundaries and twin boundaries show that they can follow $\Sigma 3\{111\}$ and $\Sigma 9\{221\}$ grain boundaries or cross $\Sigma 3\{111\}$ grain boundaries. Whether $\Sigma 3\{111\}$ GBs are crossed or not depends among other things on the orientation of the grains on either side of the twin. It demonstrates that the grain orientation relationship and not only the grain boundary character play an important role in the subgrain structure evolution and redistribution in a multicrystalline silicon ingot.

1. Introduction

Subgrain boundaries (SGBs) are known to be electrically active defects that decrease the photovoltaic (PV) efficiency and, therefore, should be limited during the manufacturing process [1]. SGBs consist of linear dislocation arrangements, as this configuration reduces the elastic energy in the crystal. In (100) grown crystals, SGBs can form during the directional solidification process by growing with the solid-liquid interface inducing a tilted subgrain structure with rotations parallel to the growth direction. The angular deviation of crystal orientations often increases with ingot height, as more dislocations of the

same character are incorporated in the SGBs [2, 3]. The orientation of the glide planes with respect to the growth direction, their activation due to equivalent resolved shear stresses during solidification, but also the generation and termination mechanisms determine the final dislocation distribution.

Subgrains are observed in all silicon ingots that are produced by casting processes for PV applications: in cast mono (cm-Si) [4-6], high-performance multicrystalline (HPmc-Si), [7] and conventional multicrystalline (mc-Si) silicon [8]. For mc-Si, either grains with $\langle 110 \rangle$ or $\langle 111 \rangle$ growth directions were reported to have the highest dislocation density [8-10]. In cast mono-Si, however, the $\langle 110 \rangle$ growth direction produced fewer dislocation clusters, i.e. narrower clusters originating at the seed junctions than the $\langle 100 \rangle$ growth direction [11].

The origin of dislocation clusters is found to be at grain boundaries [12, 13], with $\Sigma 27a$ GBs [7, 9, 14] and SGBs [15] playing a dominant role. Besides, dislocations in cast mono-Si are mainly generated at the junctions of the seed pavement [16, 17]. Additionally, subgrains originate from dislocation alignments already present in the seed crystals that can propagate into the new grown crystal during growth [18-20]. For the latter mechanism, the initial dislocation arrangement in cells in the seed is a main factor [19, 21] and depends on the stress in the seed [22-24].

Additionally, it was found that the dislocation density in the newly grown crystal is at first lower than in the un-melted seeds [17, 22]. On the one hand, it could indicate that the thermomechanical stresses imposed on the seeds during the heating process are higher than during crystallization. On the other hand, it must be considered that dislocation generation mechanisms in a seed and the newly grown crystal are different and that dislocation mobility is strongly dependent on temperature and impurities. Therefore, it is particularly important to control the crystal quality of the seeds in order to control the dislocations in the regrown part.

Just as important to understand the formation of subgrains is to find out the reason for their disappearance. A high amount of random angle GBs, like it exists in HPmc-Si, causes a decrease of the amount of subgrains in the ingot, because it is inferred that the dislocations are stopped at these boundaries [7]. It was also reported that neighbor grains with lower dislocation densities overgrow the grains with higher cluster densities [8]. These observations show that once formed, the subgrains can only be stopped by grain competition mechanisms, wherefore subgrain formation is highly undesirable in cast mono growth for which this mechanism is irrelevant due to the absence of grain boundaries.

In order to better understand the role of the seed in the formation of subgrains, small-scale directional solidification experiments using a float-zone (FZ) seed and a cast mono seed in [001] growth orientation were performed. We compare the developed grain structure by applying *in situ* X-ray diffraction imaging to monitor the solidification microstructure during growth and *ex situ* etch pit and electron backscatter diffraction (EBSD) analysis to reveal the grain structure and defect spatial distribution. Formation of SGBs in the cast mono-seeded sample is observed and discussed in terms of their formation, propagation and disappearance.

2. Experimental methods

2.1. Sample preparation and processing

Two samples originating from different processing techniques are used as seeds for directional solidification. Sample A-seed was produced by zone-melting using 9N material (SIL'TRONIX Silicon Technologies). Accordingly, the impurity concentrations of oxygen and carbon are below 10^{15} at cm^{-3} . The sample was cut with a diamond wire saw to a size of 38×7 mm and polished to a thickness of 0.3 mm. SiC abrasive paper followed by a $6 \mu\text{m}$ and a $3 \mu\text{m}$ diamond suspension was used for final polishing.

Sample B-seed was produced by the cast mono directional solidification technique from Cz seeds. The casted ingot had a laboratory scale 85 kg G2 and was provided by the Institut National de l'Energie Solaire (INES). A photoluminescence (PL) image of a vertical wafer cut from which sample B was taken is shown in Fig. 1. A white border marks the sample position (100 cm - 140 cm from the bottom). It is taken just below the area where electrically active subgrains do appear on the PL maps. In order to study subgrain influence during growth, the sample was put upside down in the furnace before partial melting. The final melt-back interface during the experiments was still above the visible subgrains and is shown in black on the magnified sample B image. The impurity content in interstitial oxygen $[O_i]$ and substitutional carbon $[C_s]$ at the height of the sample is $(6 \pm 1) \times 10^{16} \text{ cm}^{-3}$ and $(4.5 \pm 0.6) \times 10^{17} \text{ cm}^{-3}$, respectively.

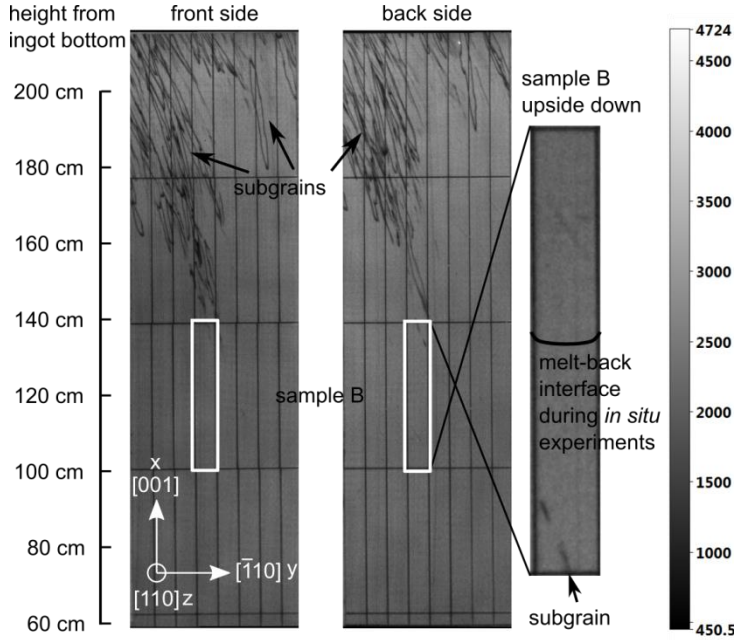


Fig. 1 Photoluminescence (PL) image of a vertical cut of the source ingot of sample B. In the upper part, electrically active SGBs are visible as dark lines. Sample B was taken just below this area.

Both samples A and B have the same crystallographic orientation. The two main surfaces are the (110) and $(\bar{1}\bar{1}0)$ planes, the vertical side planes are $(1\bar{1}0)$ and $(\bar{1}10)$ and the horizontal planes are (001) and $(00\bar{1})$.

The samples were placed in a boron nitride crucible and processed in a high temperature Bridgman furnace known as GaTSBI (Growth at high Temperature observed by Synchrotron Beam Imaging) [e.g. 25, 26]. First, the temperature of both heating elements was slowly increased from room temperature up to a temperature of 1100 °C. Then, a temperature gradient of 30 °C cm⁻¹ was applied to the heaters with $T_{\text{Top}} > T_{\text{Bottom}}$ and heating continued up to the melting point of silicon which is 1414 °C. The local vertical temperature gradient G_{local} in the sample was always lower than the applied temperature gradient G_{appl} and can be calculated with $G_{\text{local}} = T/\nu$ using the applied cooling rate \dot{T} and measuring the growth velocity of the solid-liquid interface ν [27, 28]. G_{local} was approximately $(14 \pm 3) \text{ °C cm}^{-1}$ during the experiments. When partial melting of the sample was achieved, directional solidification was triggered, for sample B by pulling the sample down with a speed of 0.03 cm min⁻¹ ($5 \times 10^{-6} \text{ m s}^{-1}$), which corresponds to a cooling rate of 0.4 °C min⁻¹, and for sample A by applying a cooling rate of 0.4 °C min⁻¹ to both heaters for the first half of solidification followed by a cooling rate of 4 °C min⁻¹ for the second half of solidification. A total of five and four heating/cooling cycles were carried out for samples A and B, leading to exposure

times to temperatures above 1100 °C of 20 and 8 hours, respectively. In this study the last heating/cooling cycle is discussed, as the grain structure is preserved for *ex situ* analysis. Although the growth processes of sample A and B differ, we do not expect significant differences during crystal growth due to the three following reasons. First, for both analyzed experiments in samples A and B, the measured growth rate (measured directly thanks to the *in situ* imaging) is identical (within the measurement accuracy limits) and the applied temperature gradient is also the same. Second, the diffraction images recorded during the first experiments using cooling rate applied to both heaters in sample B show that the general solidification features are reproducible compared to the last experiment using pulling down to initiate solidification. Third, the grain structure observed in both samples A and B is comparable.

2.2. In situ observation

In situ and real-time observation of the melting and solidification processes was achieved by using X-ray synchrotron radiation at beamline ID 19 of the European Synchrotron (ESRF) in Grenoble, France. A combination of X-ray radiography and topography imaging allows studying the development of crystal defects [29]. Two individual camera-based detector systems were used to monitor the radiographic and topographic images with an image acquisition rate of 2 s⁻¹. The radiography image contrast results from the density difference between the solid and the liquid phases and provides information on the dynamics and the morphology of the solid-liquid interface. The topography image results from Bragg diffraction and can be considered as one extended Laue spot that provides information on the crystal structure and associated extended defects. Crystal imperfections such as deformations and dislocations change the diffraction angle of the X-rays, resulting in superimpositions or gaps that are visible in the image as a change in contrast. The observed contrast provides qualitative information on the strain level which is associated with the macroscopic crystal deformation.

2.3. Ex situ analyses

After the *in situ* solidification experiments both surfaces of the samples were first polished with SiC abrasive paper and then with a 6 µm and a 3 µm diamond suspension to remove the reaction layer of the boron nitride crucible and to obtain a flat surface for EBSD analysis. EBSD was performed using a FEG-SEM JEOL JSM 7001F operating at an acceleration voltage of 20 kV, a working distance of ~20.0 mm, a tilt angle of 70° and several magnifications. The SEM was equipped with a HKL Nordlys camera driven by the ‘Channel 5’ softwares suite (comprising ‘Flamenco’ for acquisition, ‘Map Stitcher’ for stitching, ‘Tango’ for mapping and ‘Mambo’ for pole figures) using either a 7 µm or a 1 µm step size depending on the studied area. Orientation maps parallel to the growth direction (x), perpendicular to the growth direction (y) or normal to the sample surface (z) are displayed using the conventional inverse pole figure (IPF) coloring. For both samples, the x direction corresponds to the growth direction. To obtain large-scale maps, the individually scanned images were stitched together. In some cases, the individual images do not fit together perfectly, which leads to visible stitching artefacts on the large-scale maps. Grain boundaries with a special character are shown in coincidence site lattice (CSL) maps. Σ3 <111> GBs are displayed in red, Σ9 <110> GBs in blue and Σ27a <110> GBs in yellow. Σ (Sigma) is the ratio between the number of lattice points in the unit cell of the CSL lattice and the number of lattice points in the unit cell of the generating lattice. The rotations around the indicated <hkl> directions satisfy the misorientation ranges given by the Brandon criterion [30], which are (60 ± 8.66)°, (38.94 ± 5)° and (31.58 ± 2.89)° for Σ3, Σ9 and Σ27a GBs, respectively. The range within special grain boundaries are defined as Σ grain boundaries is given by $\theta = 15^\circ/\sqrt{\Sigma}$. Additionally, misorientation maps that show small angular deviations from a predefined crystallographic direction, are used to detect subgrains. The detection limit

of misorientation angles is approximately 0.5° for the EBSD analysis with the highest spatial resolution of $1\text{ }\mu\text{m}$ [31].

To reveal etch pits and grooves, the samples were etched for 5 min. with the chemical agent Sirtl ($\text{HF}(40\%):\text{CrO}_3(5\text{M}) = 1:1$). The etching revealed grain boundaries and emerging dislocations that were observed using an optical microscope. The etching was done twice: the first etching after the EBSD measurements with $7\text{ }\mu\text{m}$ resolution and the second etching after the EBSD measurements with $1\text{ }\mu\text{m}$ resolution.

3. Results

3.1. Grain structure

The overall grain structures of samples A and B are dominated by diagonal successive twinning from both edges, represented in the IPF X images of Fig. 2(a) and (c), respectively. $\Sigma 3$ twinning at the edges occurs because there exists a large undercooling [27] that facilitates the nucleation of twin grains [32]. The twin grains enter in competition at the center of the sample, though, the encounter is shifted towards the left side in both samples. From the radiographs (see Fig. 3(a) for sample A), it can be deduced that the twins nucleate earlier on the right side because the solid-liquid interface on the right side advances faster. This behavior was also reported and explained for this kind of experiments in [33]. The competition between the twins that propagate from both sides is accompanied by a significant amount of stress. This becomes clear by looking at the topography images (Fig. 3(b) and Fig. 4(a) and (b) for samples A and B, respectively), which show a very dark contrast area where the competition takes place. The dark contrast (stress) started to build up at the level of the initial solid(seed)-liquid interface. Additional dark contrast is observed on the left of Fig. 3(b), where several twinned grains nucleated as can be seen on the IPF X plot of Fig. 3(c). However, the higher stress (enhanced black contrast) is observed at the position of encounter and competition of the diagonal twins coming from the sides (Fig. 3(b)). It was also observed in our previous work [33] in comparable solidification conditions in a different sample and during another experimental campaign. In both samples the strain diminishes above in the crystal after the nucleation of a new grain (purple in IPF X map of Fig. 2(a) and (c)), which is assumed to nucleates inside a grain boundary groove created by the side twins in the sample center. It has a different crystallographic orientation than the side twins and the seed grains. Its growth direction is close to $\langle 744 \rangle$. In Fig. 3 and Fig. 4 these grains are encircled in black dotted lines. On top of them the global strain (dark contrast areas) reduces, as was previously observed in experiments with a FZ-seed of the same crystallographic orientation [33].

By looking at the IPF X and IPF Z images of both samples (Fig. 2(a)-(d)), it is apparent that the overall grain structure is the same. The $[110]$ surface direction of the seed continues in the new grains almost over the entire sample height. The main difference in the structure of both samples is the development of high, up to 3° -misorientated subgrain domains in sample B, which are not present in sample A. The subgrain domains are detectable on the EBSD orientation maps because they have slightly different crystallographic orientations compared to the grain matrix. The black lines in Fig. 2(c) and (d) and the green areas in Fig. 2(e) reveal the subgrains. Fig. 2(e) shows the degree of misorientation from the $[110]$ direction of the seed crystal in different colors: dark blue means no misorientation with respect to the reference direction and green, yellow and red mean a misorientation of 1° , 2° and 3° from the reference seed direction, respectively. The reference direction corresponds to a direction that is nearly parallel to the z-direction, i.e. normal to the sample surface.

Two subgrain domains (1 and 2) are evidenced. Considering the detection limit, the first subgrain domain becomes visible ca. 5.8 mm above the seed-regrown silicon interface and consists of two subgrains (SG1 and SG2). The second subgrain domain becomes visible ca. 12.5 mm above the seed-

regrown silicon interface and consists also of two subgrains (SG3 and SG4). The subgrains are finite and disappear again after a few millimeters.

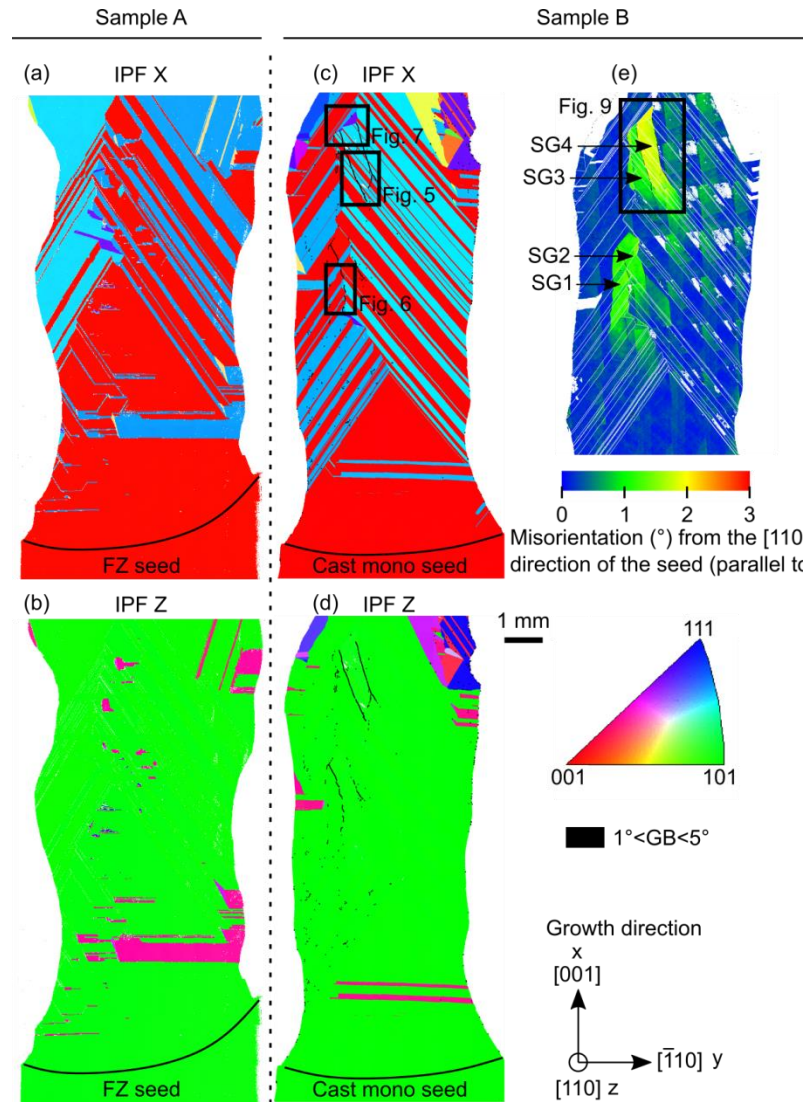


Fig. 2 (a) and (c) IPF X and (b) and (d) IPF Z orientation maps obtained by EBSD measurements of the solidified samples A (FZ-seeded) and B (cast mono-seeded), respectively. (e) The map shows the degree of misorientation from the [110] direction of the seed crystal. In sample B, SGBs are observed that show misorientations up to 2° with respect to the seed orientation (see also black-lines in (c) and (d)). The color gradations within the individual rectangles are due to map stitching artefacts and due to deviations of the electron beam during large-scale map acquisition.

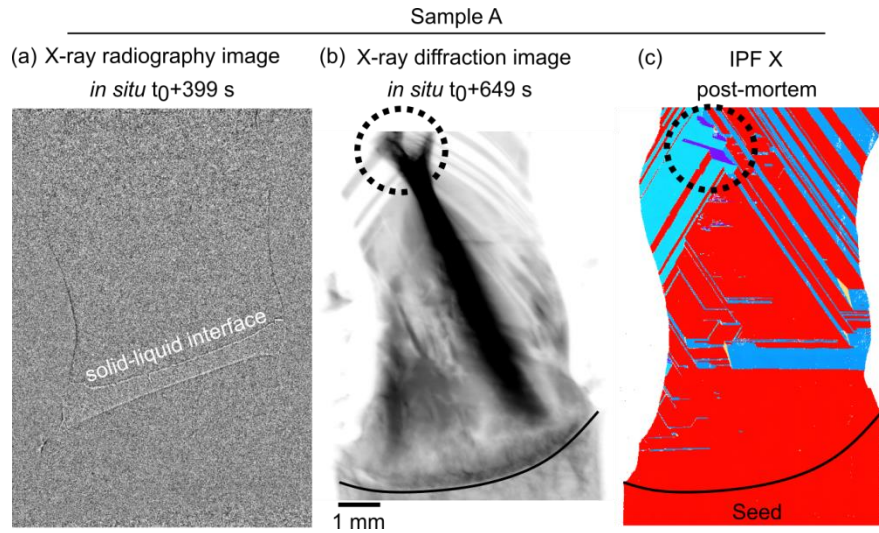


Fig. 3 (a) *In situ* X-ray radiography image, (b) *in situ* X-ray topography image and (c) post-mortem IPF X orientation map of the FZ-seeded sample A. The X-ray radiography image was post-processed to better visualize the solid-liquid interface. The dark circle indicates a new grain nucleation (purple grain in (c)), which correlates to the reduction of strain in (b). $t_0 = 0$ corresponds to the start of solidification.

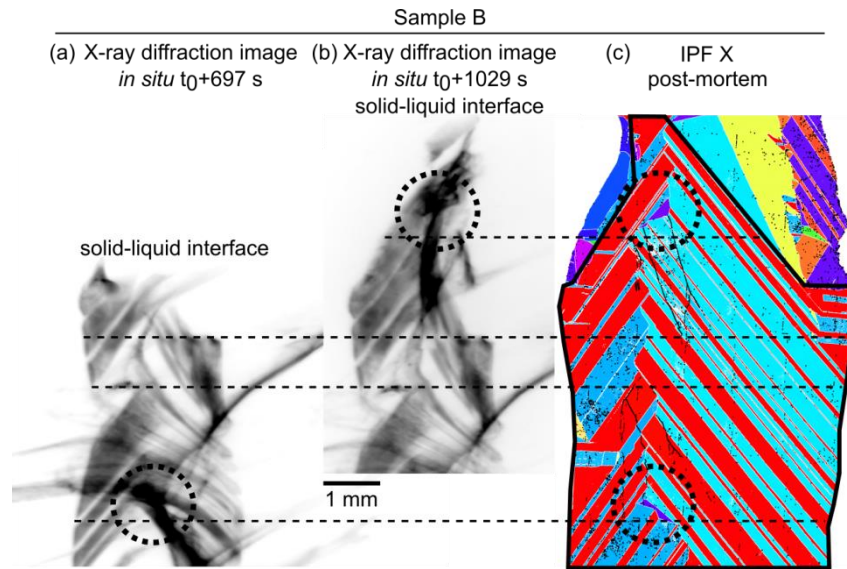


Fig. 4 (c) IPF X orientation map with (a) and (b) corresponding to *in situ* X-ray diffraction snapshots at different processing times of the cast mono-seeded sample B. $t_0 = 0$ corresponds to the start of solidification. The red [001] grains that lie in the black framed area of the orientation image are visible on the diffraction images. The circles indicate the locations of new grain nucleations (purple grains) that contribute to recovery of lower strain levels in the upper growing grains (reduction of the dark contrast area in the X-ray diffraction images). The dashed lines serve as guides to the eyes to recognize corresponding regions.

3.2. Formation of SGB domains

In Fig. 5 the formation area of subgrain 4 is shown. The CSL map (Fig. 5(a)) shows that the region consists of diagonally arranged $\Sigma 3$ twins. Figure 5(b) is an optical etch pit image on which the dark diagonal lines represent the same twin boundaries. The red dotted lines show the traces of the SGBs that

are only weakly visible or in some places are not visible at all on the microscopic image after etching (Fig. 5(b)).

On the misorientation image of Fig. 5(c), the subgrains are clearly distinguishable because they exhibit a misorientation up to 3° . The image shows the degree of misorientation from the $[110]$ direction with respect to subgrain 4. It can be seen that there is a misorientation of 3° between subgrains 3 and 4. The misorientation between subgrain 4 and the grain matrix is 1.7° . Below the sample height at which the SGBs become visible, a continuous increase of the misorientation can be measured along with the growth direction (Fig. 5(c)). Furthermore, at the lower ends of the SGBs b and c , which delimit subgrain 4, two SGB-branches initially merged into one SGB.

The misorientation angle of SGB b is the sum of the misorientation angles of the two initial branches. A summation occurred because the two branches separate subgrains that have a similar misorientation axis ($[21\bar{3}]$ compared to $[33\bar{4}]$). This supports the assumption that the two branches converged into one during solidification to form a SGB with a higher misorientation. This suggests that the dislocations incorporated in the SGB are of the same character. When the branches of SGB c merge, the misorientation is not the sum of both. The reason is that the misorientation axis of both branches differ ($[\bar{3}11]$ compared to $[\bar{1}43]$). In this case, the dislocations are probably of different character.

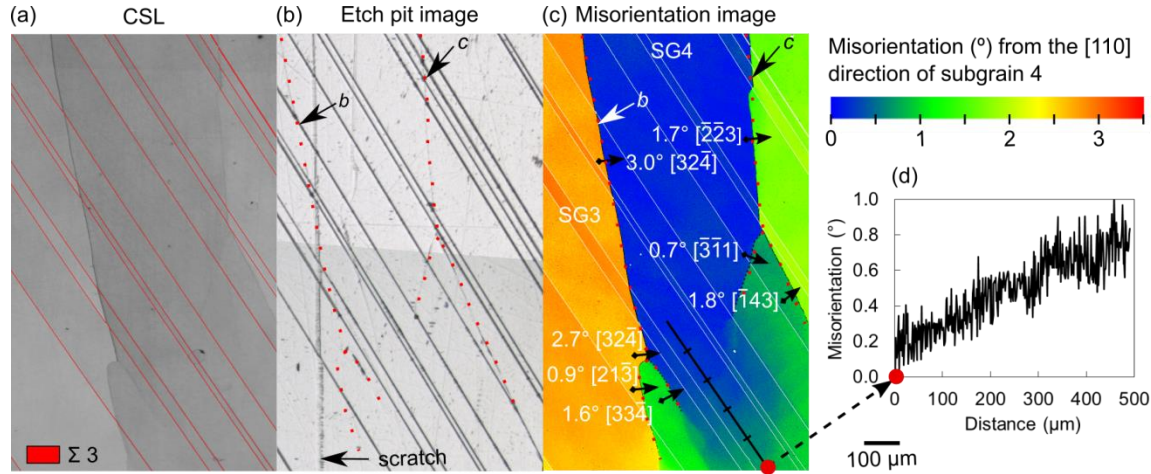


Fig. 5 (a) CSL map, (b) etch pit image and (c) misorientation map of the formation area of subgrains 3 and 4. The degree of misorientation from the $[110]$ direction of subgrain 4 is shown. (d) The graph shows a continuous increase of misorientation along the black line.

3.3. Propagation of SGBs

Once a SGB is formed, it evolves almost perpendicular to the solid-liquid interface. In Fig. 6 the propagation of SGBs d and e , which separate subgrains 1 and 2, are shown. Figure 6(a) is the CSL map and Fig. 6(b) an inverse pole figure map along the x -direction (corresponding to the growth direction). Figure 6(c) is an optical etch pit image, where the dotted red lines mark the trace of the SGBs observed with EBSD. As was shown before, the SGBs are faintly visible on the etch pit image. Figure 6(d) shows the degree of misorientation from the $[110]$ direction with respect to the grain matrix.

SGB d follows the direction of growth and crosses $\Sigma 3\{111\}$ GBs without producing noticeable changes (see dotted pentagons in Fig. 6(c)). Along some short segments, SGBs also follow $\Sigma 3\{111\}$ GBs (see dotted circle in Fig. 6(c)). It causes the $\Sigma 3$ GB $\{111\}$ to become an incoherent GB, which is expressed by the misorientation angle that deviates from 60° .

SGB e is located in a region where grain competition among grains that grow from both sides takes place. Either $\Sigma 3$ or $\Sigma 9$ GBs are formed depending on the twin relationship. A difference in the interaction

behavior between the SGB and $\Sigma 3$ and $\Sigma 9$ GBs can be seen. We find that SGBs never cross $\Sigma 9$ GBs, but follow them (see dotted rectangles in Fig. 6(b)). We also observe that the misorientation angle of SGB e increases from 1.5° to 1.8° towards the top.

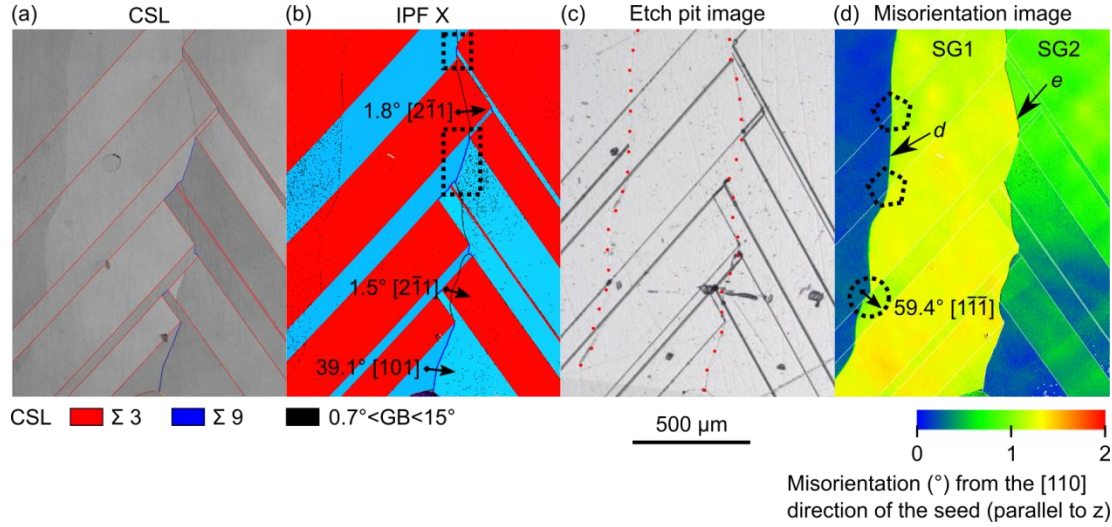


Fig. 6 (a) CSL map, (b) IPF X orientation map, (c) etch pit image and (d) misorientation map showing the interaction of SGBs with $\Sigma 3$ and $\Sigma 9$ grain boundaries.

3.4. Disappearance of SGBs

The disappearance of both subgrains 3 and 4 is associated with the nucleation of new grains of the same $\langle 744 \rangle$ type (grains I and II in Fig. 7). Nucleation of grains I and II takes place on $\Sigma 3\{111\}$ facets included within the subgrains 3 and 4, respectively. This is why they have the same crystallographic misorientation with respect to the matrix than the entire subgrain area (see Fig. 7(c)). The nucleation events of grains I and II takes place in the subgrain areas 3 and 4 on the contrary to all other previous nucleation occurring during growth. Before these nucleation events, the subgrains grew only by an upward propagation crossing grains that nucleated far away from the subgrain area (at the sides of the sample). Although grain nucleation can be triggered by the presence of dislocations and/or deformed areas [27, 33] and by extension possibly by the presence of SGBs, it is not possible to conclude on this from our experiments. Moreover, it is worth noting that the same kind of nucleation events (same crystallographic orientation and position) was observed in sample A in which SGBs were absent.

In order to understand why the subgrains disappear, it is necessary to have a detailed look at the development of the three SGBs a , b and c , which delimit subgrains 3 and 4 laterally. SGB a stops at the encounter of grain I. SGBs b and c meet the new grains I and II at a $\Sigma 3\{111\}$ GB. In both cases, they do not cross the GB but propagate along the GB inducing a direction change.

The $\Sigma 3$ GB is modified from a coherent $\Sigma 3\{111\}$ to an incoherent $\Sigma 3\{111\}$ GB. This is reflected in the misorientation angles of 56.9° (arrow 1 in Fig. 7(c)) and 58.8° (arrow 3 in Fig. 7(c)) between grains I and II and their neighbor grains, respectively, to be compared to the value of 60° expected for a perfect $\Sigma 3$ GB. These grains have a $\langle 744 \rangle$ orientation close to the growth direction. The misorientation of the incoherent $\Sigma 3$ GB below grain I is higher than that on the right side of grain II. This is due to the fact that the misorientation of SGB b is higher, too. Following the grain boundaries to the upper right, the misorientation remains unchanged. Interrupted by $\Sigma 9$ GBs, the next incoherent $\Sigma 3$ GBs have similar misorientations of 57.0° (arrow 2 in Fig. 7(c)) and 58.6° (arrow 4 in Fig. 7(c)), respectively. This is consistent with the misorientations of the SGBs measured before (3.0° and 1.1° for b and c , respectively).

Then, the SGBs encounter a triple junction between an incoherent $\Sigma 3$, and a $\Sigma 27a$ GB. In fact, it is the first time during their upward propagation that the SGBs meet a $\Sigma 27a$ GB. After the encounter they do not continue their way in the direction of growth. The formation of the $\Sigma 27a$ GBs is associated with the nucleation of the new grains I and II that form a $\Sigma 27a$ GB on top. Since $\Sigma 27a$ GBs are also observed in sample A, which has no subgrains, these $\Sigma 27a$ GBs are only the result of grain competition.

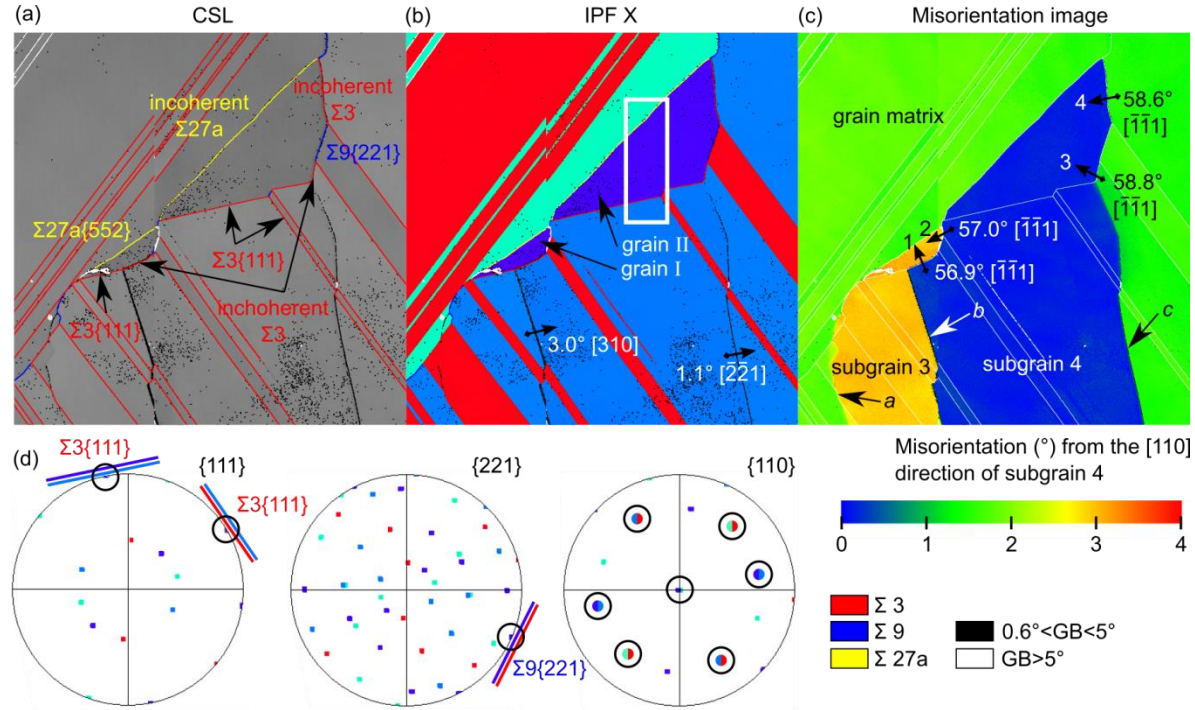


Fig. 7 (a) CSL map, (b) IPF X orientation map, (c) misorientation map and (d) $\{111\}$, $\{221\}$ and $\{110\}$ pole figures of the grains lying inside the white rectangle of map (b). The dark circles encircle common crystallographic directions.

3.5. Dislocations in the seed crystals

Dislocation distributions were observed by etching and by X-ray diffraction imaging. Dislocation densities measured by etch pit counts only show dislocations that emerge at the surface. Dislocations that stay in planes parallel to the sample surface are not revealed. In the diffraction images, dislocations are not visible if they fulfill the extinction criterion $\mathbf{b} \cdot \mathbf{g} = 0$ for the particular diffraction spot observed (\mathbf{b} is the Burgers vector and \mathbf{g} is the diffraction vector). Therefore, both techniques do not represent the total amount of dislocations, but give a qualitative indication of the amount.

Figures 8(a) and (d) show etch pit images of samples A and B at the position of the seed-regrown interface. In Fig. 8(b) and (e) *in situ* diffraction images of both samples are presented that show the seed crystals shortly before melting. The etch pits on the cast mono seed (sample B) form an array of dislocation cells. In the FZ seed the dislocation are not arranged in cells and are more widely spread. The dislocations are arranged in lines, which follow the traces of two crossing $\{111\}$ family planes that are oriented perpendicular to the surface. Finally, the dislocation density is higher in sample B-seed compared to sample A-seed.

The diffraction images confirm the observation from the etch pits images. The cast mono seed shows a dense network of dislocations arranged in cells compared to the FZ-seed. The time sequence of the *in situ* X-ray images reveal that the dislocations are not very mobile during heating and up to the melting

point in sample B compared to sample A (videos that show the heating phases of sample A and B are available as supplementary material). The two diagonal dark lines are probably micro-twins. In the FZ seed the dislocations originating from sources at the sample edges are very mobile up to the silicon melting point and move on different $\{111\}$ planes. The almost horizontal lines form because dislocations propagate on the $[111]/[\bar{1}\bar{1}\bar{1}]$ and $[\bar{1}\bar{1}\bar{1}]/[111]$ planes, whose projection traces at the surface plane are horizontal. As these planes have an angle of 35.3° with the surface $\{110\}$ planes, the movement of the dislocations on the planes can be nicely observed on the projected images. The propagation of dislocations along these planes is activated by the pressure exerted by the crucible on the main surface sides [34]. The reason for the slight inclination of the “horizontal” lines by 8° is due to a geometric distortion during recording, which is explained in [29]. Activation of the two $\{111\}$ planes that are perpendicular to the surface can only be seen close to the melting point. These are the diagonal lines ($\{111\}$ traces) that are also observed on the etch pit image.

What both samples have in common is that the etch pit density significantly reduces from the non-molten seed to the new grown crystal. In Fig. 8(c) and (f), topography images of samples A and B shortly after the first solidification cycle are shown. The seed-regrown interface is very dark and therefore distorted. Inside the new grown grains dark areas are present as well. Although individual dislocations are poorly visible, one can see that the dislocation structure is quite different in the new grown crystals: neither horizontal dislocation lines for sample A, nor dislocation cells for sample B are visible.

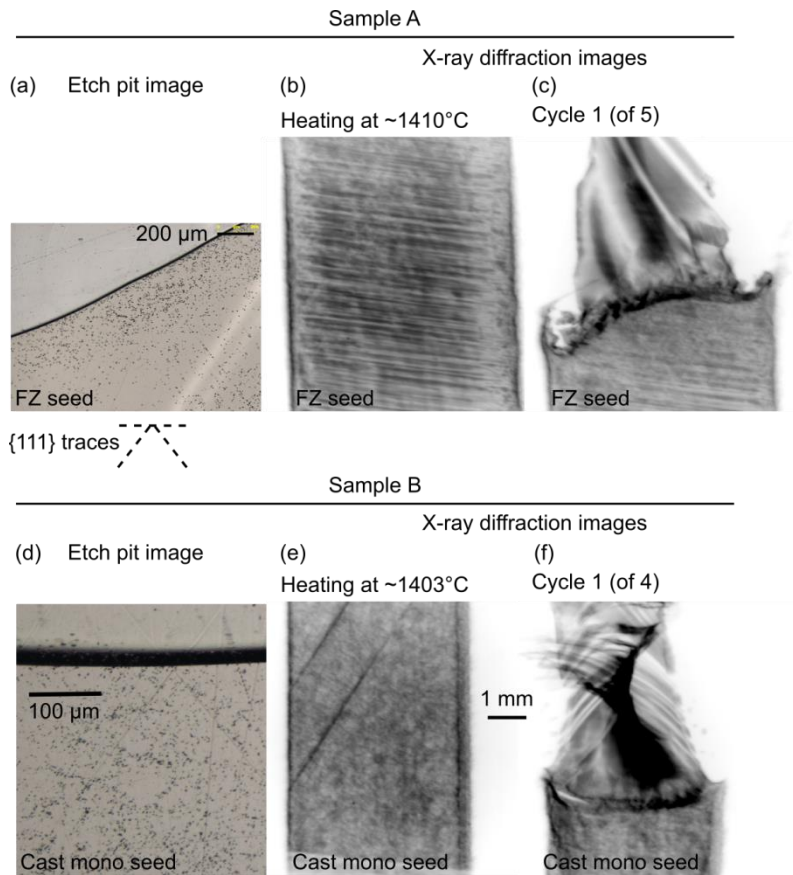


Fig. 8 (a) and (d) post-mortem etch pit images of the initial solid-liquid interface of the last cooling cycle of samples A and B, respectively. (b) and (e) X-ray diffraction images of the unmolten seeds of samples A and B, respectively, shortly before melting. (c) and (f) X-ray diffraction images after the first cooling cycles of samples A and B, respectively, that show the seeds and the regrown crystals and their different dislocation arrangements.

4. Discussion

4.1. SBG structure

4.1.1. Orientation relationship of the subgrains

The SGBs in sample B are rotated towards each other mainly by a rotation around the $[001]$ axis, i.e. the growth direction. This is illustrated in Fig. 9, where the degrees of misorientation from the $[110]$, the $[001]$ and the $[\bar{1}10]$ directions with respect to the seed orientation are shown from (a) to (c), respectively. In the x- and y-representations only the grains that have an orientation close to the original orientation of the seed can be seen in color because the other grains have a higher misorientation than 3° . The subgrains show a low misorientation along the x-direction but a similar high misorientation along the y- and z-directions consistent with tilt GBs. In Fig. 9(d) the inclination of the subgrains 3 and 4 relative to the grain matrix on both sides is schematically shown.

The fact that almost no etch pits are visible along the SGBs means that the dislocations do not emerge at the surface. Hence, it supports the point that the dislocation lines of the SGBs are mainly oriented along the growth direction. Since the rotation axis is principally along the growth direction, many dislocations have an edge character. This is consistent with the analysis of Lantreibecq et al. [18] who found that the SGBs in the source cast mono ingot are mainly composed of dislocations with a $[001]$ line character and a Burgers vector $a/2[1\bar{1}0]$. They proposed that these dislocations grow by epitaxy on the solid-liquid interface. They also found two other families of dislocations that have Burgers vectors at 45° from the growth axis. These dislocations could be responsible for deviations of the tilt direction of the subgrains also observed in this study.

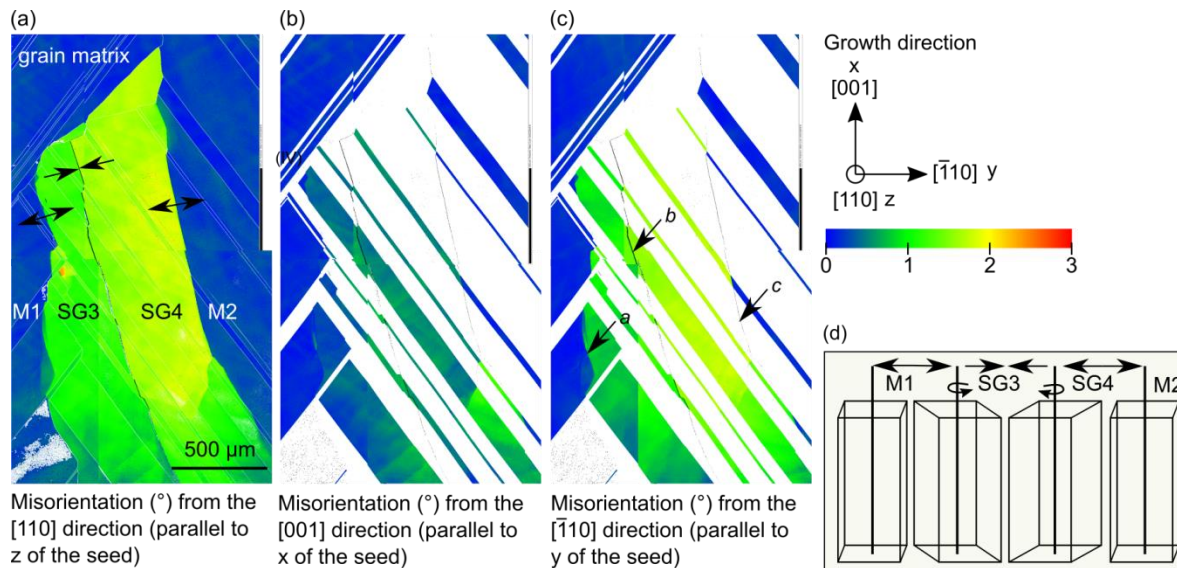


Fig. 9 Misorientation maps show the degree of misorientation from the (a) $[110]$, (b) $[001]$ and (c) $[\bar{1}10]$ direction with respect to the seed orientation. (d) Schematic representation of the tilt directions of the two subgrains SG3 and SG4 and the matrix grains on the left and right side. SGB3 and SG4 are inclined towards each other.

4.1.2. SGB misorientations and their dislocation density

For SGB *b* we observe a continuous increase of the misorientation angle in the direction of growth, which is consistent with an accumulation of dislocations in a dislocation wall. This is also supported by our observation that lower misoriented branches merge to form a higher misoriented SGB in the direction of growth (cf. Fig. 5). A similar branched structure was earlier reported by Chuang et al. who observed SGB formation in silicon *in situ* suggesting that dislocations aggregate at the solid-liquid interface and increase the misorientation angle through the continual incorporation of new dislocations [2]. The branched dislocation arrays that merge into one SGB, the increase of the SGB misorientation and their principle orientation and tilt along the growth axis suggest a SGB formation during growth. SGBs aligned along the growth direction in mc-ingots have also been reported by other authors, who also assumed a generation of dislocations during growth at the solid-liquid interface [8, 13].

The distance between individual dislocations *d* assuming that the SGB is constituted of perfect edge dislocations aligned along the SGB can be evaluated by

$$d = \mathbf{b}/\sin(\theta).$$

Using $\mathbf{b} = 0.384$ nm for the Burgers' vector magnitude in silicon along a $\langle 110 \rangle$ direction, the distance between each dislocation is $d_1 = 7.3$ nm and $d_2 = 22$ nm for θ of 3° and 1° , respectively. These misorientation angles are in the same order of magnitude as what was observed by Lantreibecq et al. in the source cast mono ingot at a height of about 160 mm from the melt-back surface [18], which is above the area where electrically active subgrains do appear on the PL maps (cf. Fig. 1). The rotation axis is also similar.

The spacing of the dislocations can be used to estimate the number of dislocations within the SGBs. With a sample thickness $t = 3 \times 10^{-2}$ cm and a dislocation spacing in the order of $d_1 = 1 \times 10^{-6}$ cm, 3×10^4 dislocations exist within SGB *b* assuming a Burgers vector of 0.384 nm standard for hypothetical edge dislocations aligned vertically constituting the boundary. Accordingly, approximately 1.5×10^4 dislocations exist in SGB *a* and *c*, respectively. This makes a total of 6×10^4 dislocations that should intersect a horizontal virtual surface to create the observed boundary misorientations.

4.2. SGB origin and implications of the crystal quality of the seeds

Oriwol et al. [12] performed a detailed study on the origin of dislocation clusters and found that 97% originate at grain boundaries. Different from this report and from other studies [e.g. 9, 35], SGBs start in the bulk crystal and not at a specific GB in our experiment. One reason for the high number of dislocations in sample B could be that dislocations propagate from the seed in the regrown crystal. Dislocation density was measured in the range 1×10^4 cm $^{-2}$ to 3×10^4 cm $^{-2}$ in another brick of the source ingot at a similar height to the one at which the sample was extracted for our experiments. Such a dislocation density results in a maximum of 540 dislocations crossing each sample horizontal surface. Compared to a number of 6×10^4 dislocations for the regrown part of sample B, the density in the seed crystal is too low to be the origin of all dislocations associated with the subgrains. Another argument against the idea that all dislocations originate from the seed is that the etch pit structure changes above the seed-regrown interface, which indicates that there is either a reduction of the total number of dislocations or a change in dislocation character and orientation or both. Hence, there are not enough dislocations in the seed to create the observed misorientations and dislocation multiplication and not only accumulation must have taken place in the regrown part.

The question arises about the reason for the dislocation generation in sample B and not in sample A. That FZ-seeded samples do not develop subgrains has been confirmed several times by similar experiments using FZ seeds [33, 36]. When considering the two seeds A and B, it is obvious that a main

difference lies in the initial dislocation density and structuration. The initial dislocation network in the cast mono seed at the melting point shows a low mobility and is arranged in a cellular structure, whereas the dislocation network in the FZ seed is very mobile and aligned on $\{111\}$ glide planes.

In comparison to the source cast mono ingot of sample B, very similar subgrains are observed indicating a similar origin. Since sample B was taken from a domain just below SGB multiplication started in the source ingot, we can conclude that subgrain formation occurs at a similar height in both cases. As only the cellular dislocation structure and microtwins are initially characterized in sample B (see Fig. 8(e)), one of those defects might carry some deformation in relation with the SGB generation. Additionally, as microtwins are not present anymore after our melting step, we hypothesize that the origin of the SGB development could be due to the cellular dislocation structure present in the seed.

Besides the dislocation structure, another difference is the chemistry of the cast mono compared to the FZ seed. The oxygen concentration in both seeds is very low, but the cast mono seed contains more carbon than the FZ seed. However, the sample is not oversaturated in carbon so that only a small number of precipitates should be present. It was reported that precipitates in the source cast mono seed do not immobilize dislocations, but that they can create dislocation cross-slip, if they are exposed to sufficient stress [18]. A strong influence of C- and N-based impurities on subgrain formation is therefore not suspected. In addition, both samples have boron concentrations $>10^{17}$ at. cm⁻³ due to contact with the boron nitride crucible. Since both samples are equally exposed to the boron nitride crucible, a different influence behavior of boron on the formation of subgrains is improbable.

The clearly different dislocation structures of the two seeds A and B indicates that it is probably the decisive factor causing the formation of subgrains. Unfortunately, it is not possible to give more information on the origin of the subgrains, because subgrains with smaller misorientations that probably exist in the lower part of the sample as it was reported in [18] could not be detected during this study due to experimental limitations. In a next step, the recording multiple diffraction spots providing complementary information is foreseen to clarify further details about the generation of subgrains.

4.3. SGB propagation and termination

The grain orientation relationship and the GB character play an important role for the propagation of the SGBs. Once the SGBs are generated, they cannot leave the sample because they grow with the solid-liquid interface and are arranged parallel to the growth direction. When meeting a grain boundary, the existence of a common slip system on both sides of the grain boundary is necessary for dislocations to cross the twin boundary. $\Sigma 3\{111\}$ GBs that separate $\{110\}<001>$ (red) and $\{110\}<221>$ (blue) oriented grains are crossed by the SGBs without inducing any visible changes (colors refer to the IPFs). $\Sigma 3\{111\}$ GBs that separate $\{110\}<221>$ (blue) and $\{110\}<744>$ (purple) oriented grains are not crossed, but change the direction of the SGBs. SGBs propagate rather along the $\Sigma 3$ and $\Sigma 9$ GBs limiting the purple grains than through the purple grains. This is plausible as dislocations can be absorbed in a GB, splitting into grain boundary dislocations (GBD) with smaller Burgers vectors, and move in the boundary [37, 38]. We observe that $\Sigma 3\{111\}$ GBs become incoherent GBs when SGBs merge with them and follow them. This observation is different from the *in situ* observations of Chuang et al., who detected only cases where SGBs crossed $\Sigma 3\{111\}$ GBs that remain coherent according to EBSD detection limits [39].

Notably, the orientation relationship of the blue and purple grains is not favorable for the dislocations in the SGB to cross. It was reported by Schmid et al. that a common slip system is not enough to explain the correlation between dislocations and grain boundaries, but that the structure of the grain boundaries has to be taken into account [40]. From a macroscopic point of view, there is no difference in the character of the crossed and uncrossed GBs. From a microscopic point of view, the GB structure is unknown and TEM measurements would be required to obtain this information. In addition, it depends on the local stress and on the type of dislocation whether it can pass through a grain boundary [41, 42]. It has

been observed [41] and simulated [43] that even $\Sigma 3\{111\}$ GBs can act as accumulation obstacles for dislocations. The stereographic projection in Fig. 7(d) shows that the common $\langle 110 \rangle$ direction of the red/blue grains is roughly oriented in the direction of the SGB path. The common $\langle 110 \rangle$ direction of the blue/purple grains, however, is almost perpendicular to the SGB direction, i.e. parallel to the solid-liquid interface. The highest probability of crossing for dislocations and thus for dislocations arranged in a SGB is obtained if there is a common glide plane (common $\langle 110 \rangle$ direction) if other conditions of stress and dislocation character are fulfilled. Consequently, as the growth direction is forced upon the grains by the temperature gradient, the unsuitable orientation of the common $\langle 110 \rangle$ direction might be the reason for the SGB change, especially if there is no Burgers vector common to both slip systems.

Above the purple grains, the SGBs do not continue their way. Either dislocations rearrange at the level of high disorder twin boundaries, like $\Sigma 27a$ GBs that limit the purple grains on top and emit new dislocations, or the dislocations leave the sample by cross slipping at the $\Sigma 3$ or $\Sigma 9$ GBs. $\Sigma 27a$ GBs have a higher boundary energy than $\Sigma 3$ and $\Sigma 9$ GBs and were found to be the source of new dislocations [13, 14, 35] probably as the result of atomic faceting [44, 45]. We do not observe any new dislocation emissions originating at these $\Sigma 27a$ GBs, but first, the *in situ* X-ray diffraction image is very dark at this position, which conceals the observation of dislocations, and second, new generated dislocations could grow out of the sample surface due to the thin sample geometry.

It is also important to note that these purple grains were identified as the grains whose nucleation releases strain previously accumulated as a result of grain competition when no SGBs are observed [33]. The new grain nucleation leads to a subsequent grain structure reorganization, which contributes to a reduction of the strain in the growing ingot. Although the disappearance of the subgrain domain is probably affected by the thin sample geometry, it means that the purple grains have an unambiguous influence on the SGB evolution. In a large-scale casting it could be a mechanism to stop or spread SGBs.

5. Conclusion

In situ growth experiments and *ex situ* analyses of two seeded wafers were performed. The initial seed orientation along the growth direction was [001] for both the FZ and the cast mono seeds. Several millimeters long subgrain boundaries, elongated in the growth direction and crossing a number of twin boundaries are formed in the cast mono-seeded sample, but not in the FZ-seeded sample. The subgrains have a main rotation axis along the [001] growth direction and increase their misorientation by merging with new SGBs appearing in their vicinity.

In situ X-ray topography imaging during the heating and solidification experiments showed that the dislocations are very mobile in the FZ seed and propagate on $\{111\}$ slip planes, whereas the dislocations in the cast mono seed are less mobile and are arranged in cells. The significantly smaller number of dislocations in the cast mono seed compared to the number of dislocations contained in the SGBs shows that dislocation multiplication mechanisms must have taken place in the regrown part. Although the source of the dislocations could not be revealed, the observations suggest that subgrain formation is related to the initial cellular dislocation structure in the cast mono seed.

Once formed, the SGBs either follow $\Sigma 9\{221\}$ and $\Sigma 3\{111\}$ GBs or cross $\Sigma 3\{111\}$ GBs. In the situation where SGBs follow twin boundaries, the coherency of the $\Sigma 3\{111\}$ GBs is degraded due to the presence of the SGBs. A particular situation is observed where a $\Sigma 3\{111\}$ GB that separates $\langle 221 \rangle$ and $\langle 744 \rangle$ oriented grains constitutes an obstacle and is not crossed by the SGBs. Whether the dislocations stop or cross-slip cannot be determined, because the sample is very thin and a change in direction of the dislocation lines would cause the dislocations to escape at the surface. However, in either of these cases the vertical SGB propagation in the growth direction is disturbed. Transferring this finding to a real size

casting, the nucleation of $\langle 111 \rangle$ oriented grains that are known to release strain could be responsible for the stopping or lateral spreading of SGBs.

Credit author statement

Maïke Becker: Conceptualization, Investigation, Writing - Original Draft, Visualization, Funding acquisition **Etienne Pihan:** Conceptualization, Investigation, Writing - Review & Editing **Fabrice Guittouneau:** Methodology, Investigation, Resources, Data Curation, Writing - Review & Editing **Laurent Barrallier:** Methodology, Resources, Writing - Review & Editing **Gabrielle Regula:** Conceptualization, Methodology, Investigation, Writing - Review & Editing **Hadjer Ouaddah:** Investigation **Guillaume Reinhart:** Investigation, Methodology **Nathalie Mangelinck-Noël:** Conceptualization, Methodology, Investigation, Data Curation, Writing - Review & Editing, Supervision, Project administration, Funding acquisition

Acknowledgements

The following funding is acknowledged: Agence Nationale de la Recherche (grant No. 14-CE05-0046-01, CrySaLID project); Deutsche Forschungsgemeinschaft (scholarship No. BE 6627/ 1-1 to Maïke Becker).

References

- [1] K.E. Ekstrøm, G. Stokkan, R. Søndena, H. Dalaker, T. Lehmann, L. Arnberg, M. Di Sabatino, Structure and dislocation development in mono-like silicon, *physica status solidi (a)*, 212 (2015) 2278-2288.
- [2] L.-C. Chuang, K. Maeda, H. Morito, K. Shiga, K. Fujiwara, Origin of small-angle grain boundaries during directional solidification in multicrystalline silicon, *Materialia*, 3 (2018) 347-352.
- [3] D. Hu, T. Zhang, L. He, H. Chen, D. Zhong, S. Cao, J. Gao, Y. Wan, The characteristics of sub-grains in the mono-like silicon crystals grown with directional solidification method, in: 38th IEEE Photovoltaic Specialists Conference, Austin, TX, 2012, pp. 002735-002738.
- [4] V.A. Oliveira, H.C. Sio, A. Faujour, L. Piot, A. Chabli, D. Camel, Recombination Activity of 2D Extended Defects in Monolike Silicon, *Energy Procedia*, 92 (2016) 755-763.
- [5] Y. Zhang, Z. Li, Q. Meng, Z. Hu, L. Liu, Distribution and propagation of dislocation defects in quasi-single crystalline silicon ingots cast by the directional solidification method, *Solar Energy Materials and Solar Cells*, 132 (2015) 1-5.
- [6] S. Zhou, C. Zhou, W. Wang, Y. Tang, J. Chen, B. Yan, Y. Zhao, Effect of Subgrains on the Performance of Mono-Like Crystalline Silicon Solar Cells, *International Journal of Photoenergy*, 2013 (2013) 1-8.
- [7] G. Stokkan, Y. Hu, Ø. Mjøs, M. Juel, Study of evolution of dislocation clusters in high performance multicrystalline silicon, *Solar Energy Materials and Solar Cells*, 130 (2014) 679-685.
- [8] D. Oriwol, M. Trempa, L. Sylla, H.S. Leipner, Investigation of dislocation cluster evolution during directional solidification of multicrystalline silicon, *Journal of Crystal Growth*, 463 (2017) 1-9.
- [9] D. Kohler, A. Zuschlag, G. Hahn, On the origin and formation of large defect clusters in multicrystalline silicon solar cells, *Solar Energy Materials and Solar Cells*, 120 (2014) 275-281.
- [10] S. Würzner, R. Helbig, C. Funke, H.J. Möller, The relationship between microstructure and dislocation density distribution in multicrystalline silicon, *Journal of Applied Physics*, 108 (2010).
- [11] F. Zhang, X. Yu, D. Hu, S. Yuan, L. He, R. Hu, D. Yang, Controlling dislocation gliding and propagation in quasi-single crystalline silicon by using $\langle 110 \rangle$ -oriented seeds, *Solar Energy Materials and Solar Cells*, 193 (2019) 214-218.
- [12] D. Oriwol, M. Hollatz, M. Reinecke, Control of Dislocation Cluster Formation and Development in Silicon Block Casting, *Energy Procedia*, 27 (2012) 66-69.

- [13] B. Ryningen, G. Stokkan, M. Kivambe, T. Ervik, O. Lohne, Growth of dislocation clusters during directional solidification of multicrystalline silicon ingots, *Acta Materialia*, 59 (2011) 7703-7710.
- [14] T. Ervik, M. Kivambe, G. Stokkan, B. Ryningen, O. Lohne, Dislocation formation at E27a boundaries in multicrystalline silicon for solar cells, in: 26th European Photovoltaic Solar Energy Conference and Exhibition, 2011, pp. 1895-1899.
- [15] M. Kivambe, G. Stokkan, T. Ervik, B. Ryningen, O. Lohne, TEM Characterization of near Sub-Grain Boundary Dislocations in Directionally Solidified Multicrystalline Silicon, *Solid State Phenomena*, 178-179 (2011) 307-312.
- [16] M.G. Tsoutsouva, V.A. Oliveira, D. Camel, J. Baruchel, B. Marie, T.A. Lafford, Mono-like silicon ingots grown on low angle misoriented seeds: Defect characterization by synchrotron X-ray diffraction imaging, *Acta Materialia*, 88 (2015) 112-120.
- [17] T. Ervik, G. Stokkan, T. Buonassisi, Ø. Mjøs, O. Lohne, Dislocation formation in seeds for quasi-monocrystalline silicon for solar cells, *Acta Materialia*, 67 (2014) 199-206.
- [18] A. Lantrebecq, J.P. Monchoux, E. Pihan, B. Marie, M. Legros, Subgrains, micro-twins and dislocations characterization in monolike Si using TEM and in-situ TEM, *Materials Today: Proceedings*, 5 (2018) 14732-14747.
- [19] A. Krause, L. Sylla, D. Oriwol, Plastic deformation as an origin of dislocations in cast mono, *Enrgy Proced*, 92 (2016) 833-838.
- [20] M. Trempa, M. Beier, C. Reimann, K. Roßhirth, J. Friedrich, C. Löbel, L. Sylla, T. Richter, Dislocation formation in seed crystals induced by feedstock indentation during growth of quasimono crystalline silicon ingots, *Journal of Crystal Growth*, 454 (2016) 6-14.
- [21] A. Lantrebecq, M. Legros, N. Plassat, J.P. Monchoux, E. Pihan, Spatial distribution of structural defects in Cz-seeded directionally solidified silicon ingots: An etch pit study, *Journal of Crystal Growth*, 483 (2018) 183-189.
- [22] V.A. Oliveira, M. Rocha, A. Lantrebecq, M.G. Tsoutsouva, T.N. Tran-Thi, J. Baruchel, D. Camel, Cellular dislocations patterns in monolike silicon: Influence of stress, time under stress and impurity doping, *Journal of Crystal Growth*, 489 (2018) 42-50.
- [23] E. Nes, Recovery Revisited, *Acta Metall Mater*, 43 (1995) 2189-2207.
- [24] G. Van Drunen, S. Saimoto, Deformation and recovery of [001] oriented copper crystals, *Acta Metallurgica*, 19 (1971) 213-221.
- [25] A. Tandjaoui, N. Mangelinck-Noel, G. Reinhart, B. Billia, X. Guichard, Twinning occurrence and grain competition in multi-crystalline silicon during solidification, *Comptes Rendus Physique*, 14 (2013) 141-148.
- [26] T. Riberi-Béridot, N. Mangelinck-Noël, A. Tandjaoui, G. Reinhart, B. Billia, T. Lafford, J. Baruchel, L. Barrallier, On the impact of twinning on the formation of the grain structure of multi-crystalline silicon for photovoltaic applications during directional solidification, *Journal of Crystal Growth*, 418 (2015) 38-44.
- [27] V. Stamelou, M.G. Tsoutsouva, T. Riberi-Béridot, G. Reinhart, G. Regula, J. Baruchel, N. Mangelinck-Noël, {1 1 1} facet growth laws and grain competition during silicon crystallization, *Journal of Crystal Growth*, 479 (2017) 1-8.
- [28] T. Riberi-Béridot, M.G. Tsoutsouva, G. Regula, G. Reinhart, I. Périchaud, J. Baruchel, N. Mangelinck-Noël, Growth undercooling in multi-crystalline pure silicon and in silicon containing light impurities (C and O), *Journal of Crystal Growth*, 466 (2017) 64-70.
- [29] M. Becker, G. Regula, G. Reinhart, E. Boller, J.-P. Valade, A. Rack, P. Tafforeau, N. Mangelinck-Noël, Simultaneous X-ray radiography and diffraction topography imaging applied to silicon for defect analysis during melting and crystallization, *Journal of Applied Crystallography*, 52 (2019) 1312-1320.
- [30] D.G. Brandon, The structure of high-angle grain boundaries, *Acta Metallurgica*, 14 (1966) 1479-1484.
- [31] F.J. Humphreys, Review - Grain and subgrain characterisation by electron backscatter diffraction, *J Mater Sci*, 36 (2001) 3833-3854.

- [32] M.G. Tsoutsouva, T. Riberi – Béridot, G. Regula, G. Reinhart, J. Baruchel, F. Guittonneau, L. Barrallier, N. Mangelinck-Noël, In situ investigation of the structural defect generation and evolution during the directional solidification of $\langle 110 \rangle$ seeded growth Si, *Acta Materialia*, 115 (2016) 210-223.
- [33] T. Riberi – Béridot, M.G. Tsoutsouva, G. Regula, G. Reinhart, F. Guittonneau, L. Barrallier, N. Mangelinck-Noël, Strain building and correlation with grain nucleation during silicon growth, *Acta Materialia*, 177 (2019) 141-150.
- [34] M.G. Tsoutsouva, T. Riberi-Béridot, G. Regula, G. Reinhart, J. Baruchel, N. Mangelinck-Noël, In Situ Imaging of Dislocation Expansion in FZ-Si Seeds During Temperature Ramp Heating Process, *physica status solidi (a)*, 215 (2018).
- [35] G. Stokkan, A. Song, B. Rynningen, Investigation of the Grain Boundary Character and Dislocation Density of Different Types of High Performance Multicrystalline Silicon, *Crystals*, 8 (2018).
- [36] H. Ouaddah, I. Périchaud, D. Barakel, O. Palais, M. Di Sabatino, G. Reinhart, G. Regula, N. Mangelinck-Noël, Role of Impurities in Silicon Solidification and Electrical Properties Studied by Complementary In Situ and Ex Situ Methods, *physica status solidi (a)*, 216 (2019).
- [37] F. van An, N.A. Bulenkov, A.V. Andreeva, Structure of a second-order twin boundary in silicon and its interaction with thermally generated lattice dislocations, *physica status solidi (a)*, 88 (1985) 429-441.
- [38] L. Priester, J. Thibault, V. Pontikis, Theoretical, Numerical and Experimental Approaches for Structural Studies of Grain Boundaries: Methods, Remarkable Results and Perspectives, *Solid State Phenomena*, 59-60 (1998) 1-50.
- [39] L.-C. Chuang, K. Maeda, H. Morito, K. Shiga, W. Miller, K. Fujiwara, Effect of misorientation angle of grain boundary on the interaction with $\Sigma 3$ boundary at crystal/melt interface of multicrystalline silicon, *Materialia*, 7 (2019).
- [40] E. Schmid, S. Würzner, C. Funke, T. Behm, R. Helbig, O. Pätzold, H. Berek, M. Stelter, The correlation between spatial alignment of dislocations, grain orientation, and grain boundaries in multicrystalline silicon, *Crystal Research and Technology*, 47 (2012) 229-236.
- [41] I. Yonenaga, K. Kutsukake, Transmission behavior of dislocations against $\Sigma 3$ twin boundaries in Si, *Journal of Applied Physics*, 127 (2020).
- [42] X. Baillin, J. Pelissier, J.J. Bacmann, A. Jacques, A. George, Dislocation transmission through $\Sigma = 9$ symmetrical tilt boundaries in silicon and germanium, *Philosophical Magazine A*, 55 (1987) 143-164.
- [43] X. Chen, L. Xiong, A. Chernatynskiy, Y. Chen, A molecular dynamics study of tilt grain boundary resistance to slip and heat transfer in nanocrystalline silicon, *Journal of Applied Physics*, 116 (2014).
- [44] A. Autruffe, V. Stenhjem Hagen, L. Arnberg, M. Di Sabatino, Dislocation generation at near-coincidence site lattice grain boundaries during silicon directional solidification, *Journal of Crystal Growth*, 411 (2015) 12-18.
- [45] A. Garg, W.A.T. Clark, J.P. Hirth, Dissociated and faceted large-angle coincident-site-lattice boundaries in silicon, *Philosophical Magazine A*, 59 (1989) 479-499.